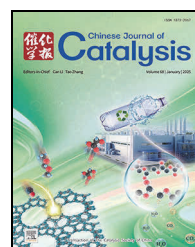
available at www.sciencedirect.comjournal homepage: www.sciencedirect.com/journal/chinese-journal-of-catalysis

Article

Efficient nitrate electroreduction to ammonia *via* synergistic cascade catalysis at Cu/Fe₂O₃ hetero-interfaces

Xiang Zhang, Weihang Li, Jin Zhang, Haoshen Zhou, Miao Zhong *

Collaborative Innovation Centre of Advanced Microstructures, National Laboratory of Solid State Microstructures, Frontiers Science Center for Critical Earth Material Cycling, College of Engineering and Applied Sciences, Nanjing University, Nanjing 210023, Jiangsu, China

ARTICLE INFO

Article history:

Received 14 September 2024

Accepted 4 November 2024

Available online 10 January 2025

Keywords:

Electrocatalysis
Reaction onset potential
Nitrate reduction to ammonia
Cascade catalysis
Heterogeneous interface

ABSTRACT

Electrochemical nitrate (NO_3^-) reduction offers a promising route for ammonia (NH_3) synthesis from industrial wastewater using renewable energy. However, achieving selective and active NO_3^- to NH_3 conversion at low potentials remains challenging due to complex multi-electron transfer processes and competing reactions. Herein, we tackle this challenge by developing a cascade catalysis approach using synergistic active sites at Cu-Fe₂O₃ interfaces, significantly reducing the NO_3^- to NH_3 at a low onset potential to about +0.4 V_{RHE}. Specifically, Cu optimizes * NO_3^- adsorption, facilitating NO_3^- to nitrite (NO_2^-) conversion, while adjacent Fe species in Fe₂O₃ promote the subsequent NO_2^- reduction to NH_3 with favorable * NO_2 adsorption. Electrochemical operating experiments, *in situ* Raman spectroscopy, and *in situ* infrared spectroscopy consolidate this improved onset potential and reduction kinetics *via* cascade catalysis. An NH_3 partial current density of ~423 mA cm⁻² and an NH_3 Faradaic efficiency (FE_{NH3}) of 99.4% were achieved at -0.6 V_{RHE}, with a maximum NH_3 production rate of 2.71 mmol h⁻¹ cm⁻² at -0.8 V_{RHE}. Remarkably, the half-cell energy efficiency exceeded 35% at -0.27 V_{RHE} (80% *iR* corrected), maintaining an FE_{NH3} above 90% across a wide range of NO_3^- concentrations (0.05–1 mol L⁻¹). Using ¹⁵N isotopic tracing, we confirmed NO_3^- as the sole nitrogen source and attained a 98% NO_3^- removal efficiency. The catalyst exhibit stability over 106-h of continuous operation without noticeable degradation. This work highlights distinctive active sites in Cu-Fe₂O₃ for promoting the cascade NO_3^- to NO_2^- and NO_2^- to NH_3 electrolysis at industrial relevant current densities.

© 2025, Dalian Institute of Chemical Physics, Chinese Academy of Sciences.

Published by Elsevier B.V. All rights reserved.

1. Introduction

Ammonia (NH_3) is a crucial chemical, widely used across industries such as fertilizers, pharmaceuticals, and textiles [1–3]. The global demand for NH_3 now exceeds 150 million tons annually, yet its production still relies on primary on the traditional Haber-Bosch process [4], which operates under extreme conditions—temperature of 400–600 °C and pressure of 200–350 atm—and results in significant carbon dioxide

 (CO_2) emissions (1.5 ton CO_2 per ton of NH_3) [5–7].

Electrocatalytic synthesis of NH_3 using renewable electricity offers a more sustainable alternative. Recently, electrocatalytic nitrogen (N_2) reduction to ammonia (NRR) has garnered considerable attention [8], but the low solubility of N_2 in water (0.02 g L⁻¹ at 20 °C at 100 kPa) and the high bond dissociation energy of $\text{N}\equiv\text{N}$ bond (941 kJ mol⁻¹) limit NRR's selectivity and energy efficiency and hinder its large-scale application [5,9,10]. In contrast, nitrate (NO_3^-) exhibits a lower bond dissociation

* Corresponding author. E-mail: miaozhong@nju.edu.cn (M. Zhong).

This work was supported by the National Natural Science Foundation of China (22272078, 22409087), the State Key Laboratory of Catalysis (2024SKL-A-016), and the "Innovation and Entrepreneurship of Talents plan" of Jiangsu Province.

[https://doi.org/10.1016/S1872-2067\(24\)60194-4](https://doi.org/10.1016/S1872-2067(24)60194-4)

energy (204 kJ mol^{-1}) and higher solubility in aqueous solutions ($383 \text{ g KNO}_3/1 \text{ L H}_2\text{O}$ at 1 atm at room temperature) [11,12]. This has led to the proposal that N_2 oxidation to NO_3^- followed by NO_3^- reduction (NO_3^- -RR) to NH_3 is kinetically more favorable, making active and energy-efficient NO_3^- to NH_3 conversion an essential goal [13].

Efforts have focused on identifying efficient single-metal catalysts for NO_3^- -RR, such as Cu [14], Co [15], Ru [16], and Fe [17,18]. Guo *et al.* [14] observed that Cu exhibits distinct catalytic behavior depending on its exposed facets and surface pH conditions, with Cu (100) excelling in strongly acidic conditions while Cu (111) facet performing better in neutral and alkaline environments. Though Cu reduce NO_3^- to nitrite (NO_2^-) efficiently [19,20], slow NO_2^- reduction kinetics limits NH_3 yield rate and Faradaic efficiency (FE) at low potentials. In contrast, Fe, Ru, and Co catalysts exhibit stronger NO_2^- reduction capabilities. Wang *et al.* [21] developed Fe single-atom catalysts showing high NO_3^- -RR activity but requiring a more negative potential in the range of -0.5 to -0.85 V versus reversible hydrogen electrode (V_{RHE}) compared to Cu catalysts. Their DFT calculations suggest that Fe has a lower energy barrier for $^*\text{NO}$ hydrogenation to $^*\text{HNO}$, but slower NO_3^- to NO_2^- reduction kinetics at low potentials.

This challenge arises from the scaling relationship limitations of intermediates adsorption on single metal catalysts [22–24]. For example, Cu binds $^*\text{O}$ intermediate ($^*\text{NO}_3$) favorably for NO_3^- to NO_2^- reduction but binding $^*\text{N}$ intermediates weakly, necessitating higher potentials to accelerate NO_2^- to NH_3 reduction. In contrast, Fe, Co, and Ni bind optimally with $^*\text{N}$ intermediates for NO_2^- to NH_3 reduction, yet their strong $^*\text{O}$ binding hinders efficient NO_2^- production [25]. To address this, researchers have developed alloy catalysts, such as CuNi and Ru doped Cu, to tune the *d*-band center and improve $^*\text{O}$ and $^*\text{N}$ intermediates adsorption [26]. However, identifying optimal bindings for both $^*\text{O}$ and $^*\text{N}$ intermediate at a single active alloy site with long-term electrochemical stability remains challenging. In addition, further improvements in NH_3 yield rate and FE at low potentials are necessary.

In this work, we present a hetero-structured Cu- Fe_2O_3 catalyst for efficient and stable NO_3^- -RR *via* synergistic catalysis. By leveraging distinct adsorption properties of $^*\text{O}$ and $^*\text{N}$ intermediates on Cu and Fe_2O_3 , we achieved continuous NO_3^- to NO_2^- and NO_2^- to NH_3 reduction *via* cascade catalysis at their interfaces, overcoming the limitations on single-metal catalysts (Fig. 1(a)). Cu facilitates NO_3^- to NO_2^- reduction, while Fe_2O_3

promotes the subsequent NO_2^- to NH_3 reduction, significantly reducing the onset potential to about $+0.4 \text{ V}_{\text{RHE}}$ for the NO_3^- -RR to NH_3 electroreduction (Fig. 1(b)). Our Cu- Fe_2O_3 catalyst delivered a NH_3 partial current density (j_{NH_3}) of 423 mA cm^{-2} and an NH_3 Faradaic efficiency (FE_{NH_3}) of 99.4% at $-0.6 \text{ V}_{\text{RHE}}$ and maximum NH_3 production rate of $2.71 \text{ mmol h}^{-1} \text{ cm}^{-2}$ at $-0.8 \text{ V}_{\text{RHE}}$. Additionally, it maintained FE_{NH_3} above 90% across a broad potential window (ranging from -0.4 to $-0.8 \text{ V}_{\text{RHE}}$) with maximum energy efficiency (EE) of 35% at $-0.27 \text{ V}_{\text{RHE}}$ ($80\% \text{ iR}$ corrected), outperforming the reported Cu, Fe, Cu-Fe combinations, and other Fe-based alloys.

In situ Raman spectroscopy revealed the formation of $^*\text{NO}_2$ and NH_3 at a low onset potential of $+0.4 \text{ V}_{\text{RHE}}$ on Cu- Fe_2O_3 catalysts, improved compared to both Cu (0.3 and $0.2 \text{ V}_{\text{RHE}}$) and Fe_2O_3 ($0.1 \text{ V}_{\text{RHE}}$) catalysts alone. Electrochemical operating experiments, *in situ* Raman spectroscopy, and *in situ* attenuated total reflection Fourier transform infrared (ATR-FTIR) spectroscopy elucidate the selective reduction and tandem catalysis mechanism of NO_3^- on the Cu- Fe_2O_3 catalyst surfaces. Furthermore, our developed catalyst exhibits robust performance for NO_3^- -RR with $\sim 95\%$ NH₃ FE across 0.05 – 1 mol L^{-1} NO₃⁻ concentrations. This study provides insights into NO₃⁻-RR kinetics in cascade catalysis, and the catalyst design is poised for efficient NH₃ electrosynthesis at low potentials and low NO₃⁻ concentrations.

2. Experimental

2.1. Materials and chemicals used for catalyst synthesis and electrochemical tests

Copper chloride dihydrate ($\text{CuCl}_2 \cdot 2\text{H}_2\text{O}$, AR) was purchased from Aladdin Scientific. Anhydrous iron chloride (FeCl_3 , 98%) was purchased from Acros Organics. Potassium hydroxide (KOH, guaranteed reagent (GR)), potassium nitrate (KNO₃, AR), sodium nitrite (NaNO₂, AR), hydrochloric acid (HCl, AR), phosphoric acid (H_3PO_4 , AR), and amidosulfonic acid ($\text{H}_3\text{NO}_3\text{S}$, AR) were purchased from Sinopharm Chemical Reagent Co., Ltd. Ammonium chloride (NH₄Cl, 99.5%), potassium sodium tartrate tetrahydrate ($\text{C}_4\text{H}_4\text{O}_6\text{KNa}$, 99%) were purchased from Shanghai Macklin Biochemical Co., Ltd. Nessler's reagent and Griess reagent were purchased from Shanghai Yuanye Bio-Technology Co., Ltd. Metal foams were purchased from Suchow Chint Co., Ltd. Nafion 117 membrane was purchased from Fuel Cell Store. All reagents were used without further

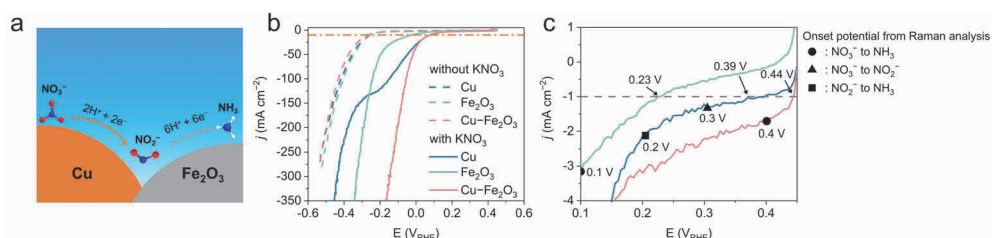


Fig. 1. (a) Schematic diagram of the cascade catalysis of NO_3^- electroreduction to NH_3 on the Cu- Fe_2O_3 electrode. (b) LSV curves comparing Cu- Fe_2O_3 , Cu, and Fe_2O_3 deposited on Ni foam in 1 mol L^{-1} KOH with 0.1 mol L^{-1} KNO₃ (solid line) and without KNO₃ (dashed line) at a scan rate of 5 mV s^{-1} ($80\% \text{ iR}$ corrected). The orange line indicates a current density of 10 mA cm^{-2} . (c) LSV curve at $+0.1$ to $+0.4 \text{ V}_{\text{RHE}}$. The gray line indicates the cathodic current density of 1 mA cm^{-2} .

purification.

2.2. Electrode preparation

The nickel foam was ultrasonically cleaned in dilute hydrochloric acid and ethanol, sequentially. Equal molar amounts of CuCl₂·H₂O and FeCl₃ were dissolved in deionized water, stirred at a speed of 800 r min⁻¹ for 10 min to ensure complete mixing, forming a precursor solution with a Cu:Fe molar ratio of 1:1. The pre-cleaned nickel foam was then immersed in the precursor solution and placed in a constant temperature oven at 105 °C overnight. After cooling to room temperature naturally, it was rinsed with deionized water and dried in an oven at 60 °C. Catalysts with different Cu/Fe ratios, including pure Cu, Cu:Fe = 1.5:1, Cu:Fe = 1:1.5, and pure Fe₂O₃, were prepared using the same method, by adjusting the molar ratio of Cu and/or Fe in the precursor solutions.

2.3. Materials characterization

Scanning electron microscopy (SEM) and energy-dispersive X-ray spectroscopy (EDS) analyses were conducted using a Hitachi SU-8100 SEM. Transmission electron microscopy (TEM) and the corresponding EDS mapping were conducted using a Tecnai F20 TEM. X-ray photoelectron spectroscopy (XPS) was performed with a PHI 5000 VersaProbe, with elements' binding energies calibrated to the C 1s peak at 284.6 eV. X-ray diffraction (XRD) analysis was conducted on a Bruker D8 Advance X-ray diffractometer using Cu K_α radiation over a 2θ range from 20° to 90° with a scan rate of 4°min⁻¹.

2.4. Electrochemical studies

Electrochemical experiments were conducted using a Metrohm Autolab electrochemical workstation in an H-cell with a three-electrode setup. The synthesized catalysts of Cu, Fe₂O₃, and Cu-Fe₂O₃ with different Cu/Fe ratios were used as working electrodes (WE). A platinum plate was used as the counter electrode (CE). Both the WE and CE were submerged in the electrolyte, with an exposed area of 1 × 1 cm². A pre-treated Nafion 117 membrane, soaked in a 0.5 mol L⁻¹ H₂SO₄ solution, separated the anode and cathode compartments. A saturated calomel electrode (SCE) in a potassium chloride saturation solution was used as the reference electrode (RE) and placed in the catholyte side. The anolyte and catholyte for NO₃⁻RR were 30 mL of 1 mol L⁻¹ KOH with KNO₃ concentrations ranging from 0.001, 0.01, 0.05, 0.1, 0.5 mol L⁻¹. Before testing, the catalysts were activated at -0.3 V_{RHE} in 1 mol L⁻¹ KOH for 10 min. For NO₃⁻RR, anolytes and catholytes were stirred at a speed of 1000 r min⁻¹ using magnetic stirrers. A potentiostatic mode was used for NO₃⁻RR at various constant potentials in the range of -0.2--0.8 V_{RHE} for 1 h. LSV was performed at a scan rate of 5 mV s⁻¹, with multiple scans until the LSV curve stabilized. To compare the experimental results, the LSV tests in different electrolytes were conducted using the same sample, not necessarily the best-performance sample. All potentials were calibrated to the RHE using the equation:

$$E_{RHE} = E_{SCE} + 0.244 \text{ V} + 0.0591 \text{ V} \times \text{pH}$$

where E_{SCE} represents the applied potential; iR compensation was applied where specified.

2.5. Product quantification

NO₃⁻, NO₂⁻, and NH₃ were quantified using ultraviolet-visible (UV-vis) spectroscopy (UV-5100). The quantification of NH₃ was verified using ¹H nuclear magnetic resonance (¹H-NMR, Agilent DD2 600 MHz). Other gaseous products were quantified using gas chromatography (GC, Agilent micro 990 with a μTCD detector).

2.5.1. NH₃ quantification using UV-vis

The NH₃ concentration was quantified using the Nessler Reagent method [27]. The electrolytes collected after 1-h electrolysis were diluted 100–500 times. Then, 1 mL of sodium potassium tartrate solution and 1 mL of Nessler's reagent were added to the sample electrolytes for chromogenic analysis with absorbance measured at a wavelength of 425 nm after keeping the sample electrolyte in the dark at room temperature for 20 min. The concentration-absorbance calibration curve was obtained using a series of standard NH₄Cl solutions (0, 0.02, 0.04, 0.08, 0.1, 0.2 mmol L⁻¹) in 1 mol L⁻¹ KOH.

2.5.2. NO₂⁻ quantification using UV-vis

After 1-h electrolysis, the electrolyte was collected and diluted 500–2000 times. Then, 0.7 mL of phosphoric acid solution and 1 mL of Griess reagent were added for chromogenic analysis. The absorbance was measured at 540 nm after keeping the sample electrolytes in the dark at room temperature for 20 min. The concentration-absorbance calibration curve was obtained using a series of standard NaNO₂ solutions (0, 0.29, 0.58, 1.16, 2.9, 7.25 μmol L⁻¹) in 1 mol L⁻¹ KOH.

2.5.3. NO₃⁻ quantification using UV-vis

After 1-h electrolysis, the electrolyte was collected and diluted 500–2000 times. Then, 1 mL of 0.1 mol L⁻¹ HCl and 0.1 mL of sulfamic acid reagent (0.8 wt%) were added for chromogenic analysis. The absorbance was measured at 220 and 275 nm after keeping the sample electrolytes in the dark at room temperature for 15 min. The absorbance is calculated as:

$$A = A_{220} - 2A_{275}$$

The concentration-absorbance calibration curve was obtained using a series of standard KNO₃ solutions (0, 0.01, 0.02, 0.04, 0.06, 0.08 mmol L⁻¹) in 1 mol L⁻¹ KOH.

2.5.4. NH₃ quantification using ¹H-NMR

Dimethyl sulfoxide (DMSO) was used as the internal standard. The internal standard was prepared by diluting DMSO (30 μL) with deionized water to 1000 times its original volume, resulting in a 1/1000 (v/v) DMSO solution. The NMR sample is prepared by dissolving standard ammonium chloride solutions of different concentrations in deionized water and adjusting the pH = 2 using dilute hydrochloric acid. A liquid sample (1 mL) was mixed uniformly with D₂O (200 μL) and 1/1000 DMSO (100 μL), and then placed into an NMR tube. The concentra-

tion-peak area calibration curve was obtained using a series of standard NH₄Cl solutions (0, 50, 100, 150, 200 mmol L⁻¹) in 1 mol L⁻¹ KOH.

NH₃ yield rate and FE were calculated using the following equations:

$$\text{Yield} = C_{\text{NH}_3} \times V / (S \times t)$$

where C_{NH_3} is the concentration of the product in mmol L⁻¹; V is the volume of the cathodic electrolyte in mL; S is the area of the cathodic catalyst in cm⁻²; t is the reaction time in h;

$$\text{FE}_{\text{NH}_3} = \frac{nC_{\text{NH}_3}VF}{Q} \times 100\%$$

where n is the number of electrons transferred; F is the Faraday constant (96485 C mol⁻¹); Q is the total charge passed in C.

The half-cell energy efficiency (EE) was calculated using the following equation:

$$\text{EE}_{\text{NH}_3} = (1.23V_{\text{RHE}} - E_{\text{NH}_3}^{\theta}) \times \text{EF}_{\text{NH}_3} / (1.23V_{\text{RHE}} - E_{\text{NH}_3})$$

where 1.23 V_{RHE} is the theoretical potential for OER; $E_{\text{NH}_3}^{\theta}$ is the theoretical potential for NO₃⁻RR ($E_{\text{NH}_3}^{\theta} = 0.69$ V_{RHE}); E_{NH_3} is the working potential for NO₃⁻RR.

The NO₃⁻ removal was calculated using the following equations:

$$\text{NO}_3^- \text{ removal} = (C_{\text{before}}(\text{NO}_3^-) - C_{\text{after}}(\text{NO}_3^-)) / C_{\text{before}}(\text{NO}_3^-) \times 100\%$$

where $C_{\text{before}}(\text{NO}_3^-)$ is the NO₃⁻ concentration before the reaction in mmol L⁻¹; $C_{\text{after}}(\text{NO}_3^-)$ is the NO₃⁻ concentration after the reaction in mmol L⁻¹.

2.6. In situ Raman measurements

In situ Raman measurements were conducted using an Xpiora Plus Raman spectrometer in a home-made electrolysis cell. The laser wavelength was 638 nm and the laser intensity was set at 10%. The synthesized catalysts used as the working electrode, an Ag/AgCl electrode was used as the reference electrode, and a platinum plate was used as the counter electrode. The electrolyte was 1 mol L⁻¹ KOH containing 0.1 mol L⁻¹ KNO₃. All experiments were performed at room temperature. Raman spectra were acquired by accumulating 10 measurements, each with an exposure time for 5 s.

2.7. In situ ATR-FTIR measurements

In situ ATR-FTIR analyses were performed using a Thermo Scientific Nicolet iS20 FTIR spectrometer. The ECIR-II cell used in the tests was bought from the Shanghai Linglu Instrument & Equipment Co., Ltd. The synthesized catalysts were used as the working electrode, pressed onto a silicon prism using a glassy carbon electrode. An Ag/AgCl electrode was used as the reference electrode, and a platinum wire was used as the counter electrode. A 1 mol L⁻¹ KOH aqueous electrolyte containing 0.1 mol L⁻¹ KNO₃ was used as the electrolyte. All measurements were conducted at room temperature. All spectra were acquired by averaging 32 scans at a resolution of 4 cm⁻¹.

3. Results and discussion

In a three-electrode H-type cell, we evaluated the electro-

chemical NO₃⁻RR performance of the Cu, Fe₂O₃, and Cu-Fe₂O₃ catalysts synthesized via hydrothermal growth on Ni foams. Pure Ni foam has been reported to be relatively inert for NO₃⁻RR [28,29], but it works as an electrically conductive substrate with a high surface area. We first studied the NO₃⁻RR performance in 1 mol L⁻¹ KOH electrolytes in an LSV mode from +0.45 to -0.55 V_{RHE} at the scanning rate of 5 mV s⁻¹. All potentials on the LSV curves have been 80% iR corrected. As shown in Fig. 1(b), the addition of NO₃⁻ led to a notable increase in current density, indicating NO₃⁻ was reduced on these electrodes.

On Cu catalyst, two peaks showing apparent current densities appeared: NO₃⁻ to NO₂⁻ at +0.2 to -0.2 V_{RHE} and NO₂⁻RR beyond -0.3 V_{RHE}, with a plateau between -0.2 to -0.3 V_{RHE} indicating effective NO₃⁻ to NO₂⁻ reduction but slow NO₂⁻ reduction on Cu. This result is confirmed by the LSV result of Cu in a NO₂⁻ solution showing a more negative onset potential of ~-0.15 V_{RHE} (Fig. 2(a)). In contrast, Fe₂O₃ did not show NO₂⁻ accumulation, indicating a stronger NO₂⁻ to NH₃ conversion ability. NO₂⁻ was rapidly reduced to NH₃ once generated. This result is consistent with the LSV result of Fe₂O₃ catalyst in a NO₂⁻ solution showing a more positive onset potential of > 0.3 V_{RHE} (Fig. 2(b)). Cu-Fe₂O₃ exhibits similar onset potentials in the range of 0.15 to 0.4 V_{RHE} in both NO₃⁻ and NO₂⁻ solutions (intermediates and NH₃ was observed 0.4 V_{RHE} in Raman spectroscopy, and apparent current density for the NO₃⁻ to NH₃ conversion was observed at ~0.15 V_{RHE}), suggesting efficient conversion of both species. On Cu-Fe₂O₃, NO₃⁻RR performance is close to NO₂⁻RR performance, indicating that NO₂⁻ generated on Cu species was effectively reduced on Fe₂O₃ (Fig. 2(c)).

In comparison with Cu (0.078 V_{RHE} @10 mA cm⁻²) and Fe₂O₃ (-0.026 V_{RHE} @10 mA cm⁻²), the Cu-Fe₂O₃ exhibited a more positive potential of 0.08 V_{RHE} at 10 mA cm⁻² and a higher current density of greater than 350 mA cm⁻² at -0.2 V_{RHE}. Additionally, it is worth mentioning that the NO₃⁻RR activity for the bare Ni foam (23 mA cm⁻² at -0.2 V_{RHE}) is markedly lower compared to the catalysts loaded samples (Fig. S1).

The Tafel slope of Cu-Fe₂O₃ (129.14 mA dec⁻¹) is lower than that of Cu (248.79 mA dec⁻¹) and Fe₂O₃ (259.81 mA dec⁻¹) in Fig. 2(d), consolidating that Cu-Fe₂O₃ exhibits faster electron transfer kinetics and higher NO₃⁻RR activity [30]. The results from electrochemical impedance spectroscopy (EIS) supported this finding (Fig. S2 and Table S1), showing that Cu-Fe₂O₃ has a smaller charge transfer resistance (R_{ct}) for NO₃⁻RR compared to Cu and Fe₂O₃. Additionally, we found that the NO₃⁻RR performance is diffusion-controlled (Figs. S3 and S4), with a marked increase in NO₃⁻RR current density upon the addition of stirring. Subsequently, 1-h NO₃⁻RR performance evaluations were conducted at different potentials with a rotation speed at 1000 rpm to minimize the impact of diffusion. The liquid-phase products (NH₃ and NO₂⁻), were quantitatively analyzed using the Nessler's reagent method and Griess reagent method with ultraviolet-visible (UV-vis) spectroscopy [27] (Figs. S5-S7).

Electrochemical NO₃⁻RR performance results for different catalysts at same potential revealed that Cu-Fe₂O₃ exhibited the highest current density (~423 mA cm⁻²), FE_{NH3} (99.4%), and yield rate of NH₃ (1.96 mmol h⁻¹ cm⁻²) at -0.6 V_{RHE} (Figs.

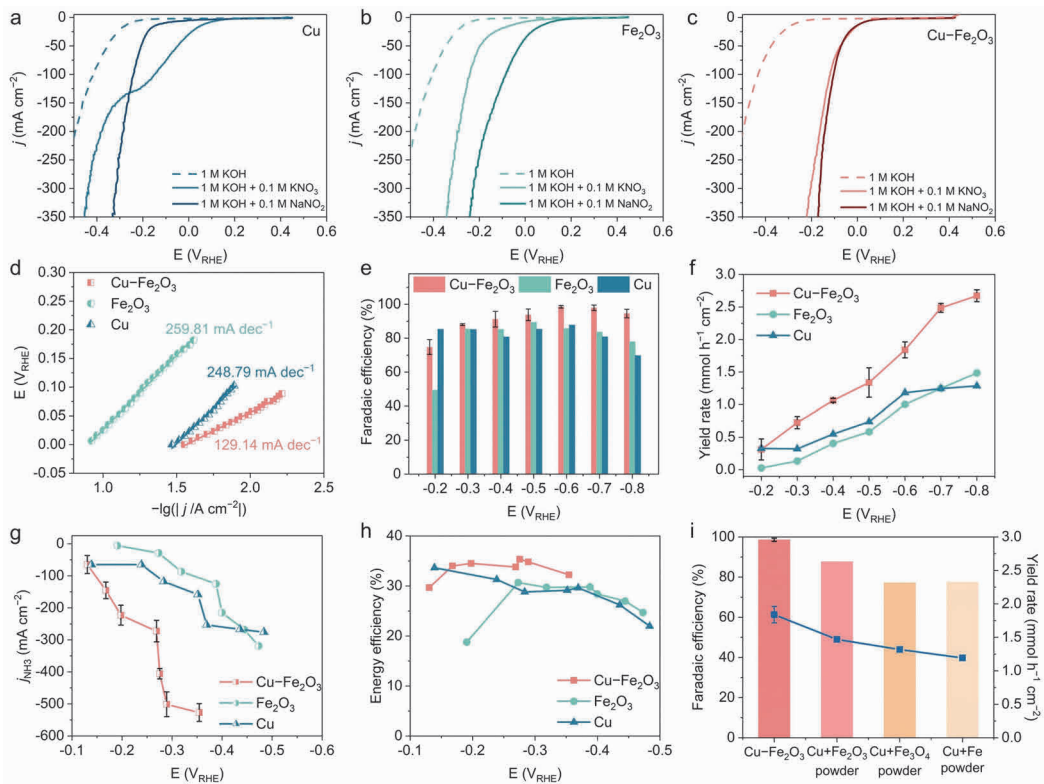


Fig. 2. Electrochemical analysis of NO_3^- -RR using $\text{Cu}-\text{Fe}_2\text{O}_3$, Cu, and Fe_2O_3 catalysts loaded on Ni foams. LSV curves of Cu (a), Fe_2O_3 (b), and $\text{Cu}-\text{Fe}_2\text{O}_3$ (c) catalysts on Ni foams in 1 mol L^{-1} KOH and 0.1 mol L^{-1} KNO_3 (80% iR corrected). (d) Tafel slopes of Cu, Fe_2O_3 , and $\text{Cu}-\text{Fe}_2\text{O}_3$ catalysts on Ni foams in 1 mol L^{-1} KOH and 0.1 mol L^{-1} KNO_3 . FE (e) and yield rate (f) of NH_3 for the catalysts at different potentials. (g) Partial current densities of NH_3 (80% iR corrected) at different potentials with different catalysts. (h) EE of NH_3 (80% iR corrected) with different catalysts. (i) FE and yield rate of NH_3 for catalysts with different valence states of Fe species combined with Cu at $-0.6 \text{ V}_{\text{RHE}}$.

2(e)–(g)), compared to Cu (1.18 mmol $\text{h}^{-1} \text{cm}^{-2}$, 87.73%) and Fe_2O_3 (1.00 mmol $\text{h}^{-1} \text{cm}^{-2}$, 85.74%) (Figs. S8–S10). We utilized GC to quantify the gaseous products resulting from NO_3^- -RR at $-0.6 \text{ V}_{\text{RHE}}$, which showed a ~1% H_2 FE, with no other N -containing gas-phase by-products, such as N_2 , N_2O , and NO (Fig. S11). Additionally, $\text{Cu}-\text{Fe}_2\text{O}_3$ demonstrated a higher NH_3 partial current density than Cu and Fe_2O_3 across a wide potential range (Figs. S12 and S13), exceeding -400 mA cm^{-2} at a low applied potential of $-0.6 \text{ V}_{\text{RHE}}$, and exceeding -500 mA cm^{-2} at $-0.29 \text{ V}_{\text{RHE}}$ (80% iR corrected). Moreover, $\text{Cu}-\text{Fe}_2\text{O}_3$ showed a higher EE compared to Cu and Fe_2O_3 , achieving a maximum of 35% EE at $-0.27 \text{ V}_{\text{RHE}}$ (80% iR corrected) in Fig. 2(h). Screening the Cu/Fe ratios in $\text{Cu}-\text{Fe}_2\text{O}_3$ catalysts revealed a volcano trend for the NH_3 production performance (Figs. S14 and S15), with the optimal performance at a Cu:Fe ratio of 1:1. The EIS test results indicate that compared to Cu ($R_{\text{ct}} = 17.2 \Omega$), Fe_2O_3 ($R_{\text{ct}} = 30.0 \Omega$), Cu:Fe = 1.5:1 ($R_{\text{ct}} = 16.2 \Omega$), and Cu:Fe = 1:1.5 ($R_{\text{ct}} = 12.4 \Omega$), with the smallest R_{ct} (10.5 Ω) for Cu:Fe = 1:1 (Figs. S2 and S16). The LSV curves corroborated these findings (Fig. S17), indicating that the synergy on Cu and Fe species at an optimal ratio is important for active NO_3^- RR. Subsequently, we investigated the NO_3^- -RR performance of Fe with different valence states combined with Cu (Fig. 2(i)), and found that Fe^{3+} ($\text{Cu}+\text{Fe}_2\text{O}_3$ powder) exhibited a NH_3 FE of ~87% with a NH_3 yield rate of 1.46 mmol $\text{h}^{-1} \text{cm}^{-2}$, greater than those of $\text{Cu}+\text{Fe}_3\text{O}_4$ powder (~77%, 1.31 mmol $\text{h}^{-1} \text{cm}^{-2}$) and $\text{Cu}+\text{Fe}$

powder (~77%, 1.19 mmol $\text{h}^{-1} \text{cm}^{-2}$).

To explore the evolution of reactants, intermediates, and products during NO_3^- -RR on $\text{Cu}-\text{Fe}_2\text{O}_3$, Cu, and Fe_2O_3 catalysts, we conducted *in situ* Raman studies in a homemade H-type cell (Fig. S18). As shown in Figs. 3(a)–(c), at the open circuit potential (OCP) and $0.4 \text{ V}_{\text{RHE}}$ on all catalysts, characteristic Raman peaks at $\sim 1049 \text{ cm}^{-1}$ attributed to the symmetric stretching of NO_3^- were observed [31]. At potentials of $0.4 \text{ V}_{\text{RHE}}$ or more cathodic, Raman peaks corresponding to the symmetric and antisymmetric chelated nitro groups of $^*\text{NO}_2$ at ~ 1125 and $\sim 1243 \text{ cm}^{-1}$ [32], respectively, and the N=O stretching vibration of the bridging nitro group at $\sim 1445 \text{ cm}^{-1}$ [28,33] were observed on $\text{Cu}-\text{Fe}_2\text{O}_3$ (Fig. 3(a)), indicating the occurrence of $^*\text{NO}_2^-$ adsorption on the catalyst surface. At further reduced potential of $0.1 \text{ V}_{\text{RHE}}$ or more cathodic, the symmetric stretching of $^*\text{NO}_3^-$ appeared at 1028 cm^{-1} , which aligns with the prior result [28]. On the other hand, the Raman characteristic peak corresponding to the symmetric bending vibration of $^*\text{HNH}$ appeared near 1374 cm^{-1} from $0.4 \text{ V}_{\text{RHE}}$, indicating the onset of hydrogenation of N -containing intermediates [33]. Similarly, the signal corresponding to the antisymmetric bending vibration of the HNH group in the product NH_3 appeared near 1580 cm^{-1} from $0.4 \text{ V}_{\text{RHE}}$ and gradually intensified at more negative potentials [34]. At $-0.1 \text{ V}_{\text{RHE}}$, peaks appeared that may correspond to NH_2OH at 1160 cm^{-1} [35], while the peaks at 1197 and 1275 cm^{-1} are attributed to the $^*\text{O}-\text{NO}$ and the antisymmetric chelated nitro

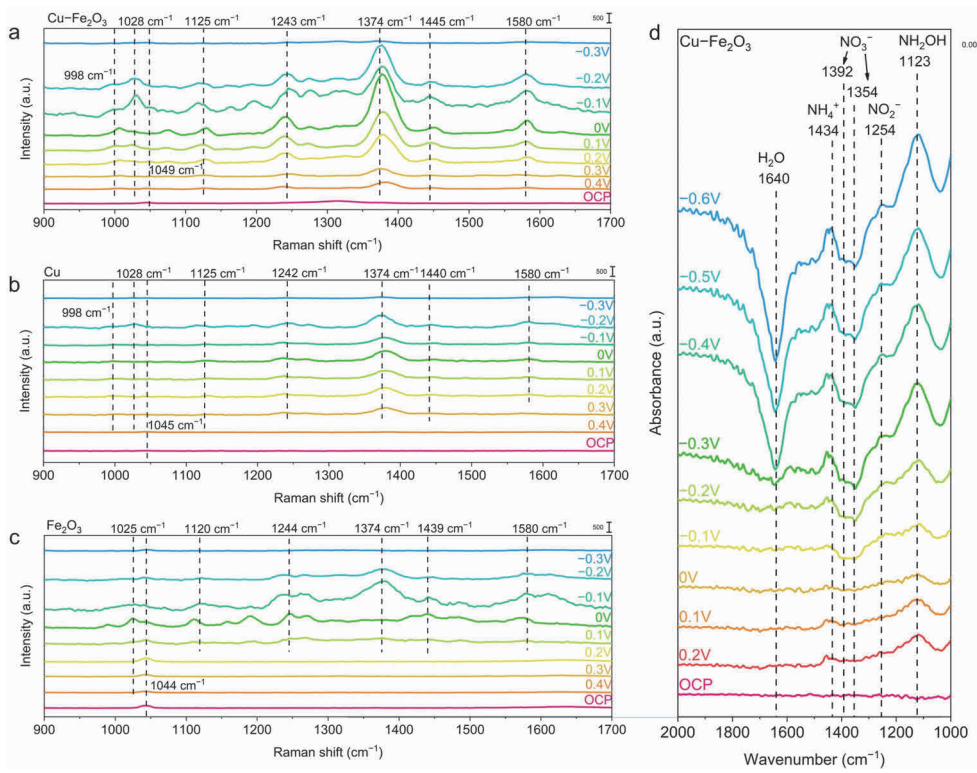


Fig. 3. *In situ* Raman spectra at various potentials of Cu-Fe₂O₃ (a), Cu (b), and Fe₂O₃ (c). (d) *In situ* FTIR spectroscopy of Cu-Fe₂O₃ in 1 mol L⁻¹ KOH and 0.1 mol L⁻¹ KNO₃.

groups *ONO* of NO₂⁻ [36], respectively. Also note that at potentials more negative than -0.3 V_{RHE}, the hydrogen evolution reaction (HER) was enhanced, producing H₂ bubbles that weakens Raman signals.

Cu (Fig. 3(b)) and Fe₂O₃ (Fig. 3(c)) catalysts exhibited Raman peaks during NO₃⁻RR. The onset potential of NO₂⁻ peaks on Cu (0.3 V_{RHE}) were more positive compared to that on Fe₂O₃ (0.1 V_{RHE}), indicating improved kinetics in reducing NO₃⁻ to NO₂⁻ on Cu. The onset potentials for the appearance of NO₂⁻ and NH₃ peaks on Fe₂O₃ were identical (0.1 V_{RHE}), 0.3 V more negative than that on Cu-Fe₂O₃. This result is in consistent with the LSV curves in Fig. 2(b) that reducing NO₃⁻ to NO₂⁻ is the limiting step.

We further employed electrochemical *in situ* ATR-FTIR spectroscopy with a thin-layer internal reflection Otto mode to analyze the reactants, intermediates, and products during the NO₃⁻RR. The ATR-FTIR setup is shown in Fig. S19. The FTIR spectra represent the relative changes in absorbance, where downward bands indicate the consumption of reactants, and upward bands indicate the formation of intermediates or products. As shown in Fig. 3(d), downward absorption bands at 1354 and 1392 cm⁻¹ attributed to the asymmetric and symmetric stretching vibrations of the N-O bond in NO₃⁻ [37] were observed on Cu-Fe₂O₃ at 0.2 V_{RHE}, indicating a significant amount of NO₃⁻ consumption. The stretching vibrations of the N-O bond in NH₂OH [28,38], antisymmetric stretching vibration of the N-O bond in NO₂⁻ [38], and N-H vibration in NH₄⁺ [39] were observed at 1123, 1254, and 1434 cm⁻¹, respectively, indicating the significant formation of NO₂⁻ and NH₃. FTIR confirmed the NO₃⁻ to NO₂⁻, and NO₂⁻ to NH₃ reduction steps.

The NO₃⁻RR trends on Cu, Fe₂O₃, and Cu-Fe₂O₃ are first examined using density functional theory (DFT) calculations (Fig. S30). Optimized structures of each intermediate adsorbed for NO₃⁻RR on catalysts are shown in Fig. S31. On Cu, the rate-determining step is the *NO to *NOH conversion (0.85 eV), indicating that the *NO₂ to NH₃ process on Cu is relatively difficult. Conversely, on Fe₂O₃, the rate-determining step is the NO₃^{*} to NO₃H* process (0.96 eV), suggesting that the *NO₃ to *NO₂ process is more challenging. On Cu-Fe₂O₃, the reaction energy for *NO to *NOH at the Cu site of the interface decreases from 0.85 eV (Cu) to 0.56 eV, and the free energy for the *NO₃ to *NO₃H process at the Fe site of the interface decreases from 0.96 eV (Fe₂O₃) to 0.67 eV. The migration of *NO₂ to the Fe site (with a migration free energy of -0.37 eV, suggesting the process is energetically favorable) allows the *NO₂ to *NH₃ process to proceed more favorably at the Fe site. Thus, the relay catalysis is more likely to occur at the interface with improved kinetics, which is consistent with our experimental conclusions (Fig. S30(b)).

Fig. 4(a) shows that NH₃-related UV-vis absorbance signals at 425 nm were detected after one hour of reduction at -0.6 V_{RHE} with the presence of KNO₃ in the electrolyte. The NH₃ yield rate was estimated ~1.96 mmol h⁻¹ cm⁻² via NO₃⁻ electroreduction on Cu-Fe₂O₃ (Fig. S20). This result is confirmed by analyzing the ¹H-NMR spectra of the NO₃⁻RR reduction electrolyte using ¹⁴NO₃ and ¹⁵N-labeled ¹⁵NO₃⁻ isotope sources (Fig. S21). The NMR spectra demonstrated distinct peaks at 6.83, 6.96, and 7.09 δ corresponding to ¹⁴NH₄⁺ when K¹⁴NO₃ was employed and peaks at 6.86 and 7.05 δ corresponding to ¹⁵NH₄⁺ when K¹⁵NO₃ was utilized (Fig. 4(b)). Quantitatively, the NMR

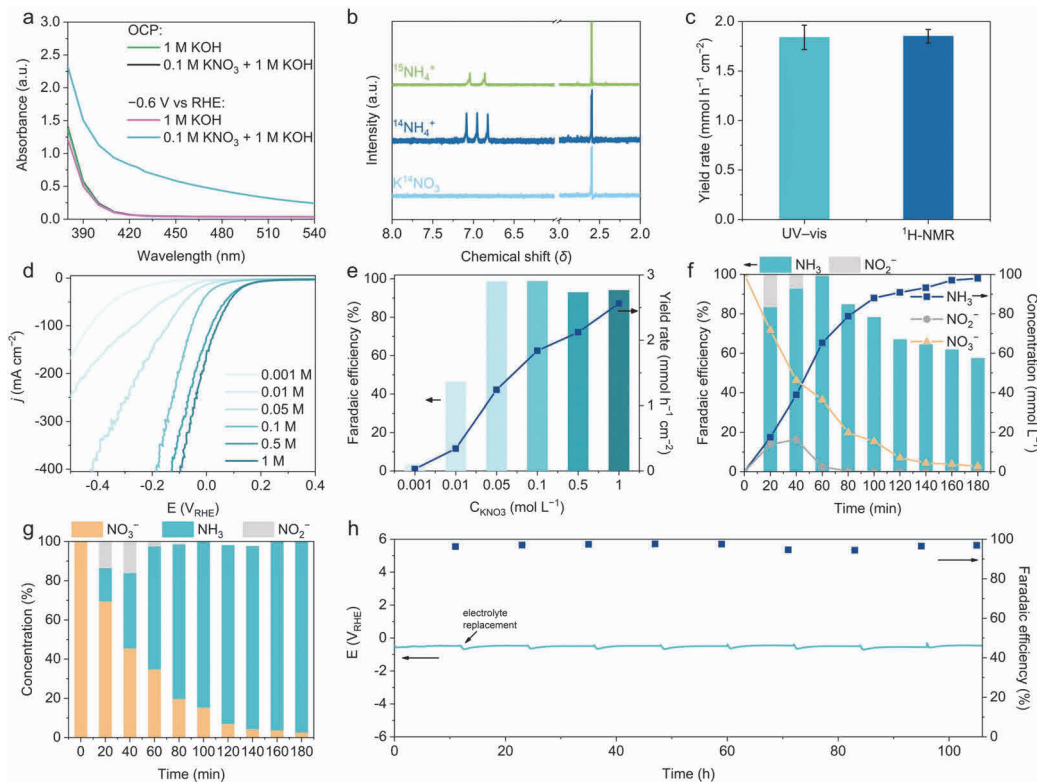


Fig. 4. Electrochemical NO₃⁻RR performance on Cu-Fe₂O₃ electrodes. (a) UV-vis absorption spectra of the electrolytes after the reduction reaction in 1 mol L⁻¹ KOH with and without 0.1 mol L⁻¹ KNO₃ at -0.6 V_{RHE} and at OCP. The electrolyte was diluted to 500 times in volume before measurement. (b) ¹H-NMR spectra of the NO₃⁻RR electrolyte using K¹⁴NO₃ and K¹⁵NO₃ as the N source in 1 mol L⁻¹ KOH electrolyte at -0.6 V_{RHE}. The reduction reaction was performed for 1 h. (c) NH₃ yield rates at -0.6 V_{RHE}, measured using Nessler's reagent method and ¹H-NMR spectroscopy. (d) LSV curves of Cu-Fe₂O₃ electrodes with different KNO₃ concentrations in 1 mol L⁻¹ KOH (80% iR corrected). (e) NH₃ FE and yield rate of Cu-Fe₂O₃ at -0.6 V_{RHE}. (f) The time-dependent concentrations of NO₃⁻, NO₂⁻ and NH₃ and the corresponding FE during the NO₃⁻RR process on Cu-Fe₂O₃ at -0.6 V_{RHE}. (g) The time-dependent concentrations of NO₃⁻, NO₂⁻ and NH₃ during the NO₃⁻RR process using Cu-Fe₂O₃ at -0.6 V_{RHE}. (h) NO₃⁻RR durability test using Cu-Fe₂O₃ at -400 mA cm⁻² in 1 mol L⁻¹ KOH + 1 mol L⁻¹ KNO₃.

spectra results are also consistent with the UV-vis results (Fig. 4(c)).

We extended our electrochemical NO₃⁻RR with different NO₃⁻ concentrations, from 0.001 to 1 mol L⁻¹, mimicking the NO₃⁻ concentrations of 0.88 mmol L⁻¹ to 1.95 mol L⁻¹ in wastewater [40]. The LSV results indicated that the current density improved with the increase in KNO₃ concentration (Fig. 4(d)), suggesting enhanced kinetics at a higher NO₃⁻ concentration. The NH₃ yield rate increased from 0.03 to 2.57 mmol h⁻¹ cm⁻² with the increase of KNO₃ concentration from 0.001 to 1 mol L⁻¹. Notably, at the NO₃⁻ concentration higher than 0.05 mol L⁻¹, the FE_{NH3} exceeded 90% (Fig. 4(e)), suggesting that the coverage of NO₃⁻ on catalysts play an essential role in the NO₃⁻RR kinetics.

Fig. 4(f) shows the NO₃⁻ removal and nitrogen species transformation over time. After 180 min, 98% NO₃⁻ was completely converted into NH₃. Further, the concentrations of NO₃⁻, NO₂⁻, and NH₃ at different NO₃⁻RR operation time were elucidated in Fig. 4(f). Over the course of 180 min, a mere 2.70 mmol L⁻¹ of residual NO₃⁻ was observed. Fig. 4(g) illustrates the NO₃⁻ conversion over time, underscoring the high efficiency of the Cu-Fe₂O₃ catalyst in converting NO₃⁻ and NO₂⁻ into NH₃. Our stability tests, conducted at a constant current of -400 mA cm⁻² in 1 mol L⁻¹ KOH and 1 mol L⁻¹ KNO₃ electrolyte, revealed that

the FE of NH₃ remained above 94%, with only minimal degradation of < 5% over a continuous 106-h electrolysis period (Fig. 4(h)). We also conducted a stability test at a constant potential of -0.6 V_{RHE} in a 1 mol L⁻¹ KOH + 0.1 mol L⁻¹ KNO₃ electrolyte for 20-h. The FE and yield rate of NH₃ remained above 94% and 1.5 mmol h⁻¹ cm⁻², respectively (Fig. S22).

A comprehensive characterization of the post-reaction Cu-Fe₂O₃ catalysts were performed. SEM images illustrated that the Cu and Fe₂O₃ catalysts loaded on the Ni foam manifested distinct morphologies of flakily structured Cu and dispersed particulate Fe₂O₃ on Ni foams, respectively (Figs. S23(a) and S23(d)). The Cu-Fe₂O₃ displayed an interlinked particulate structure, with an enhanced degree of particle interconnection as the proportion of Cu precursor increased (Fig. 5(a) and Fig. S23). EDS mappings confirmed the homogeneous distribution of Fe₂O₃ and Cu within the Cu-Fe₂O₃ structure (Fig. S24). Inductively coupled plasma optical emission spectroscopy (ICP-OES) and EDS analysis corroborated a consistent Cu to Fe elemental ratio in the Cu-Fe₂O₃ catalyst (Table S2).

High-resolution TEM (HRTEM) images and corresponding EDS mappings identified the presence of mixed Cu-Fe₂O₃ nanoparticles (Figs. 5(b)–(d)). Notably, the HRTEM image in Fig. 5(b) revealed a distinct Cu-Fe₂O₃ interface, displaying lattice fringes with spacings of Cu (200) and Cu (111) planes at 0.17

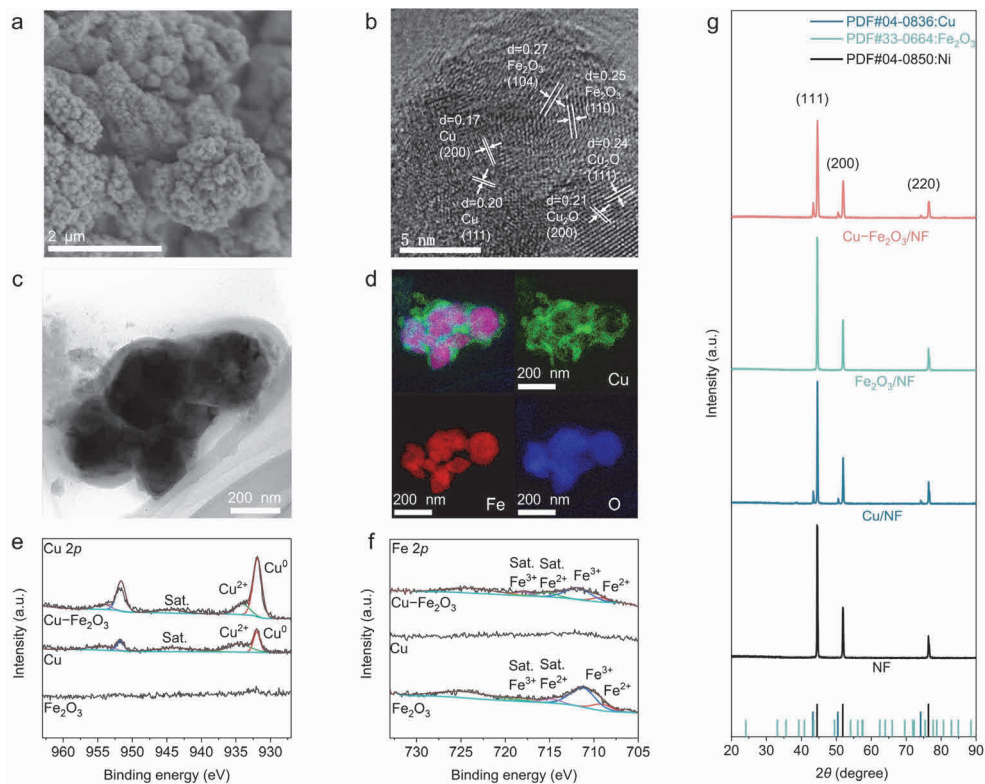


Fig. 5. Structure and composition characterization of the Cu-Fe₂O₃ catalyst after the 1-h NO₃⁻RR. (a) SEM images of the Cu-Fe₂O₃ catalyst. (b-d) HRTEM images and the corresponding EDX elemental mapping images of Cu-Fe₂O₃. Fe 2p (e) and Cu 2p (f) narrow-scan XPS spectra of Cu-Fe₂O₃. (g) XRD patterns of Cu-Fe₂O₃, Cu, and Fe₂O₃ loaded on Ni foam.

and 0.20 nm, and the Fe₂O₃ (104) and Fe₂O₃ (110) planes at 0.27 and 0.25 nm. Additionally, the (111) and (200) planes of Cu₂O at 0.24 and 0.21 nm were discernible, suggesting the presence of partially oxidized Cu on the surfaces.

XPS analyses studied the chemical states of Cu and Fe on catalyst surfaces. The XPS survey spectra (Fig. S25) and Cu 2p narrow-scan spectrum (Fig. 5(e)) revealed that Cu primarily exists as metallic Cu⁰ (931.9 eV) along with Cu²⁺ (934.5 eV), attributing to partial surface oxidation. Conversely, the Fe 2p narrow-scan spectrum (Fig. 5(f)) indicated that Fe primarily exists in the oxidized state as Fe³⁺ (711.3 eV), with a minor presence of Fe²⁺ 2p peaks (709.5 eV). The XPS analysis underscored the proportions of Fe³⁺ and Fe²⁺ as 85.7% and 14.3% in Cu-Fe₂O₃ (Table S2), respectively. Notably, shifts in the Fe 2p and Cu 2p peaks to higher and lower binding energies, respectively, in the Cu-Fe₂O₃ catalyst compared to individual oxides, suggesting an electron transfer from Fe to Cu [41].

The surface composition of the catalysts was further identified using Raman spectroscopy (Fig. S26). Both Cu-Fe₂O₃ and Fe₂O₃ exhibit peaks characteristic of the α-Fe₂O₃ phase, including one A_{1g} symmetry species at 221 cm⁻¹ and three E_g symmetry species at 288, 406, and 609 cm⁻¹ [42]. Additionally, a Fe₃O₄ peak at ~671 cm⁻¹ on the Cu-Fe₂O₃ catalyst [43] displayed a redshift relative to the Fe₂O₃ catalyst, likely due to Cu incorporation affecting the lattice vibrational frequency [44]. A common peak at ~470 cm⁻¹ in all catalysts was attributed to α-SiO_x present in the test matrix [45]. The consistency of Raman signals for Cu with those of Ni foam suggested that the Cu

loaded on the Ni foam predominantly existed in the metallic state. XRD results confirmed the presence of metallic Cu in the bulk phases of both Cu-Fe₂O₃ and the Cu catalyst (Fig. 5(g)), displaying pronounced diffraction peaks at 43.66°, 50.85°, and 74.57°, corresponding to the (111), (200), and (220) facets of face-centered cubic Cu (PDF#04-0836), respectively. However, due to the overriding signal intensity from the Ni foam, characteristic diffraction signals of Fe and its oxides were not discernible in both Cu-Fe₂O₃ and Fe₂O₃ samples. Post-reaction characterizations of the Cu-Fe₂O₃ catalyst via SEM, XRD and XPS (Figs. S27-S29) showed that the morphology, bulk state, and surface composition remained essentially consistent with those observed prior to the reaction.

4. Conclusions

In this study, we designed cascade catalysis at the Cu-Fe₂O₃ interface that leads to outstanding electrochemical NO₃⁻RR performance with a reduced onset potential. The developed Cu-Fe₂O₃ catalyst delivered a NH₃ partial current density exceeding 420 mA cm⁻² at -0.27 V_{RHE} (80% iR corrected), with a half-cell EE of 35%, and achieved high NH₃ FE exceeding 90% across a broad range of NO₃⁻ concentrations (0.05–1 mol L⁻¹). *In situ* Raman, *in situ* ATR-FTIR spectroscopy, and electrochemical studies consolidate the cascade catalysis of NO₃⁻ to NO₂⁻ on Cu, followed by the reduction of NO₂⁻ to NH₃ on Fe₂O₃ with a much-reduced onset potential to +0.4 V_{RHE}. Our research not only elucidates the cascading synergistic effect between Cu

and Fe_2O_3 but also proposes an approach for designing dual-site catalyst for the electrochemical conversion of complex molecules via cascade catalysis with favorable reaction kinetics.

Conflicts of Interest

The authors declare no competing financial interest.

Electronic supporting information

Supporting information is available in the online version of this article.

References

- [1] W. Li, H. Jiang, X. Zhang, B. Lei, L. Li, H. Zhou, M. Zhong, *J. Am. Chem. Soc.*, **2024**, 146, 21968–21976.
- [2] Z. Deng, J. Liang, Q. Liu, C. Ma, L. Xie, L. Yue, Y. Ren, T. Li, Y. Luo, N. Li, B. Tang, A. Ali Alshehri, I. Shakir, P. O. Agboola, S. Yan, B. Zheng, J. Du, Q. Kong, X. Sun, *Chem. Eng. J.*, **2022**, 435, 135104.
- [3] L. Ouyang, J. Liang, Y. Luo, D. Zheng, S. Sun, Q. Liu, M. S. Hamdy, X. Sun, B. Ying, *Chin. J. Catal.*, **2023**, 50, 6–44.
- [4] J. G. Chen, R. M. Crooks, L. C. Seefeldt, K. L. Bren, R. M. Bullock, M. Y. Darenbourg, P. L. Holland, B. Hoffman, M. J. Janik, A. K. Jones, M. G. Kanatzidis, P. King, K. M. Lancaster, S. V. Lymar, P. Pfromm, W. F. Schneider, R. R. Schrock, *Science*, **2018**, 360, eaar6611.
- [5] W. Chen, X. Yang, Z. Chen, Z. Ou, J. Hu, Y. Xu, Y. Li, X. Ren, S. Ye, J. Qiu, J. Liu, Q. Zhang, *Adv. Funct. Mater.*, **2023**, 33, 2300512.
- [6] J. Zhao, L. Liu, Y. Yang, D. Liu, X. Peng, S. Liang, L. Jiang, *ACS Sustainable Chem. Eng.*, **2023**, 11, 2468–2475.
- [7] L. Li, A. Ozden, S. Guo, F. P. García de Arquer, C. Wang, M. Zhang, J. Zhang, H. Jiang, W. Wang, H. Dong, D. Sinton, E. H. Sargent, M. Zhong, *Nat. Commun.*, **2021**, 12, 5223.
- [8] X. Fu, J. B. Pedersen, Y. Zhou, M. Saccoccia, S. Li, R. Sažinas, K. Li, S. Z. Andersen, A. Xu, N. H. Deissler, J. B. V. Mygind, C. Wei, J. Kibsgaard, P. C. K. Vesborg, J. K. Nørskov, I. Chorkendorff, *Science*, **2023**, 379, 707–712.
- [9] D. Hao, Z.-g. Chen, M. Figiela, I. Stepnjak, W. Wei, B.-J. Ni, *J. Mater. Sci. Technol.*, **2021**, 77, 163–168.
- [10] T. Xie, X. He, L. He, K. Dong, Y. Yao, Z. Cai, X. Liu, X. Fan, T. Li, D. Zheng, S. Sun, L. Li, W. Chu, A. Farouk, M. S. Hamdy, C. Xu, Q. Kong, X. Sun, *Chin. Chem. Lett.*, **2024**, 35, 110005.
- [11] D. R. Lide, *CRC Handbook of Chemistry and Physics, 85th edition*, CRC press, **2004**, 4–77.
- [12] X. Fan, L. Xie, J. Liang, Y. Ren, L. Zhang, L. Yue, T. Li, Y. Luo, N. Li, B. Tang, Y. Liu, S. Gao, A. A. Alshehri, Q. Liu, Q. Kong, X. Sun, *Nano Res.*, **2022**, 15, 3050–3055.
- [13] K. Dong, Y. Yao, H. Li, H. Li, S. Sun, X. He, Y. Wang, Y. Luo, D. Zheng, Q. Liu, Q. Li, D. Ma, X. Sun, B. Tang, *Nat. Synth.*, **2024**, 3, 763–773.
- [14] T. Hu, C. Wang, M. Wang, C. M. Li, C. Guo, *ACS Catal.*, **2021**, 11, 14417–14427.
- [15] K. Yang, S.-H. Han, C. Cheng, C. Guo, T. Li, Y. Yu, *J. Am. Chem. Soc.*, **2024**, 146, 12976–12983.
- [16] Y. Yao, L. Zhao, J. Dai, J. Wang, C. Fang, G. Zhan, Q. Zheng, W. Hou, L. Zhang, *Angew. Chem. Int. Ed.*, **2022**, 61, e202208215.
- [17] J. Lin, X. Lin, S. Lu, W. Liao, T. Qi, S. Liang, Z.-J. Zhao, L. Jiang, *Chem. Eng. Sci.*, **2024**, 300, 120664.
- [18] Z. Sun, J. Lin, S. Lu, Y. Li, T. Qi, X. Peng, S. Liang, L. Jiang, *Langmuir*, **2024**, 40, 5469–5478.
- [19] Y. Liu, J. Wei, Z. Yang, L. Zheng, J. Zhao, Z. Song, Y. Zhou, J. Cheng, J. Meng, Z. Geng, J. Zeng, *Nat. Commun.*, **2024**, 15, 3619.
- [20] Y. Nie, H. Yan, S. Lu, H. Zhang, T. Qi, S. Liang, L. Jiang, *Chin. J. Catal.*, **2024**, 59, 293–302.
- [21] Z.-Y. Wu, M. Karamad, X. Yong, Q. Huang, D. A. Cullen, P. Zhu, C. Xia, Q. Xiao, M. Shakouri, F.-Y. Chen, J. Y. Kim, Y. Xia, K. Heck, Y. Hu, M. S. Wong, Q. Li, I. Gates, S. Siahrostami, H. Wang, *Nat. Commun.*, **2021**, 12, 2870.
- [22] J. Zhang, C. Guo, S. Fang, X. Zhao, L. Li, H. Jiang, Z. Liu, Z. Fan, W. Xu, J. Xiao, M. Zhong, *Nat. Commun.*, **2023**, 14, 1298.
- [23] X. Yu, Y. Xu, L. Li, M. Zhang, W. Qin, F. Che, M. Zhong, *Nat. Commun.*, **2024**, 15, 1711.
- [24] M. Zhong, K. Tran, Y. Min, C. Wang, Z. Wang, C.-T. Dinh, P. De Luna, Z. Yu, A. S. Rasouli, P. Brodersen, S. Sun, O. Voznyy, C.-S. Tan, M. Askerka, F. Che, M. Liu, A. Seifitokaldani, Y. Pang, S.-C. Lo, A. Ip, Z. Ulissi, E. H. Sargent, *Nature*, **2020**, 581, 178–183.
- [25] W. Gao, K. Xie, J. Xie, X. Wang, H. Zhang, S. Chen, H. Wang, Z. Li, C. Li, *Adv. Mater.*, **2023**, 35, 2202952.
- [26] Y. Wang, A. Xu, Z. Wang, L. Huang, J. Li, F. Li, J. Wicks, M. Luo, D.-H. Nam, C.-S. Tan, Y. Ding, J. Wu, Y. Lum, C.-T. Dinh, D. Sinton, G. Zheng, E. H. Sargent, *J. Am. Chem. Soc.*, **2020**, 142, 5702–5708.
- [27] L. Zhou, C. E. Boyd, *Aquaculture*, **2016**, 450, 187–193.
- [28] J.-Y. Fang, Q.-Z. Zheng, Y.-Y. Lou, K.-M. Zhao, S.-N. Hu, G. Li, O. Akdim, X.-Y. Huang, S.-G. Sun, *Nat. Commun.*, **2022**, 13, 7899.
- [29] Y. Zhang, Y. Zhao, Z. Chen, L. Wang, P. Wu, F. Wang, *Electrochim. Acta*, **2018**, 291, 151–160.
- [30] L. Liu, S.-J. Zheng, H. Chen, J. Cai, S.-Q. Zang, *Angew. Chem. Int. Ed.*,

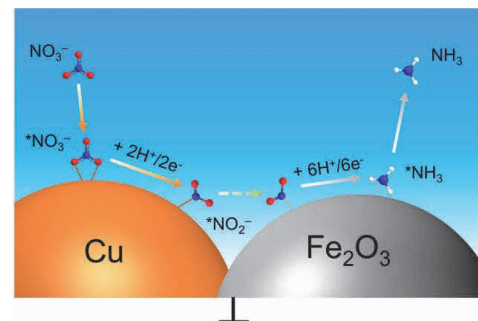
Graphical Abstract

Chin. J. Catal., 2025, 68: 404–413 doi: 10.1016/S1872-2067(24)60194-4

Efficient nitrate electroreduction to ammonia via synergistic cascade catalysis at Cu/ Fe_2O_3 hetero-interfaces

Xiang Zhang, Weihang Li, Jin Zhang, Haoshen Zhou, Miao Zhong *
Nanjing University

The Cu- Fe_2O_3 catalyst enhances NO_3^- to NH_3 electroreduction through cascade catalysis, leveraging near-optimal $^*\text{NO}_3^-$ adsorption on Cu and near-optimal $^*\text{NO}_2^-$ on Fe_2O_3 , achieving high NH_3 Faradaic efficiency and yield rate with low onset potential.



- 2024**, 63, e202316910.
- [31] Z. Zhou, G. G. Huang, T. Kato, Y. Ozaki, *J. Raman Spectrosc.*, **2011**, 42, 1713–1721.
- [32] D. M. L. Goodgame, M. A. Hitchman, *Inorg. Chem.*, **1965**, 4, 721–725.
- [33] D. P. Butcher, A. A. Gewirth, *Nano Energy*, **2016**, 29, 457–465.
- [34] N. Wen, M. H. Brooker, *J. Phys. Chem.*, **1995**, 99, 359–368.
- [35] L. Li, C. Wan, S. Wang, X. Li, Y. Sun, Y. Xie, *Nano Lett.*, **2024**, 24, 2392–2399.
- [36] Y. Kim, J. Ko, M. Shim, J. Park, H.-H. Shin, Z. H. Kim, Y. Jung, H. R. Byon, *Chem. Sci.*, **2024**, 15, 2578–2585.
- [37] M. C. Figueiredo, J. Souza-Garcia, V. Climent, J. M. Feliu, *Electrochem. Commun.*, **2009**, 11, 1760–1763.
- [38] T. Zhang, J. Lv, R. Yang, Z. Yan, X. Sun, X. Xu, Y. Liu, *Adv. Energy Mater.*, **2024**, 14, 2400790.
- [39] S. Lu, G. Lin, H. Yan, Y. Li, T. Qi, Y. Li, S. Liang, L. Jiang, *ACS Catal.*, **2024**, 14, 14887–14894.
- [40] P. H. van Langevelde, I. Katsounaros, M. T. M. Koper, *Joule*, **2021**, 5, 290–294.
- [41] C. Wang, Z. Liu, T. Hu, J. Li, L. Dong, F. Du, C. Li, C. Guo, *ChemSusChem*, **2021**, 14, 1825–1829.
- [42] M. Srivastava, A. K. Ojha, S. Chaubey, J. Singh, P. K. Sharma, A. C. Pandey, *J. Alloys Compd.*, **2010**, 500, 206–210.
- [43] D. Giuntini, E. Torresani, K. T. Chan, M. Blankenburg, L. Saviot, B. Bor, B. Domènec, M. Shachar, M. Müller, E. A. Olevsky, J. E. Garay, G. A. Schneider, *Nanoscale Adv.*, **2019**, 1, 3139–3150.
- [44] E. Guerrero, D. A. Strubbe, *J. Phys. Chem. C*, **2022**, 126, 18393–18403.
- [45] T. Mueller, S. Schwertheim, W. R. Fahrner, *J. Appl. Phys.*, **2010**, 107, 014504.

Cu/Fe₂O₃异质界面协同级联催化硝酸盐高效电还原为氨

张 翔, 李苇杭, 张 进, 周豪慎, 钟 苗*

南京大学现代工程与应用科学学院, 先进微结构协同创新中心, 固体微结构国家实验室,
地球关键材料循环前沿科学中心, 江苏南京210023

摘要: 氨(NH₃)是一种重要的化学品, 广泛用于合成化肥、药品、纺织品和其他行业。传统Haber-Bosch工艺用于NH₃合成, 该工艺需高温高压条件。另一方面, 工业废水中的过量硝酸盐(NO₃⁻)会导致水体污染。通过电催化手段, 可以高效率、高选择性的将NO₃⁻还原为NH₃, 不仅能够处理环境问题, 还提供了一种绿色可持续的NH₃合成途径。然而, NO₃⁻还原(NO₃⁻RR)过程复杂, 涉及8电子和9质子的转移, 并可能伴随强烈的析氢竞争反应(HER)。单一金属催化剂难以在低电位下同时具备对NO₃⁻和亚硝酸根(NO₂⁻)的高效吸附和还原能力。

针对该问题, 本文设计了Cu-Fe₂O₃异质结构催化剂, 利用其界面上的双位点有效分步催化实现NO₃⁻到NO₂⁻和NO₂⁻到NH₃的电还原过程。扫描电镜、透射电镜、X-射线衍射和X-射线光电子能谱等表征手段证实了Cu和Fe₂O₃在泡沫镍基底上的致密生长, 并确定了其价态和体相组成。在0.1 mol L⁻¹ KNO₃和1 mol L⁻¹ KOH的电解液中, Cu-Fe₂O₃在-0.27 V_{RHE}下展示了接近100%的NH₃法拉第效率, 并在-0.35 V_{RHE}下实现了2.71 mmol h⁻¹ cm⁻²的高NH₃产率, 远超单独使用Cu或Fe₂O₃催化剂的性能。同时, -0.27 V_{RHE}下的半池能量效率超过35%, 且在宽NO₃⁻浓度范围内(0.05–1 mol L⁻¹), NH₃选择性均保持在90%以上。通过¹⁵N同位素标记确定了氮源完全来自KNO₃。计时电流测试表明, 反应3 h后, NO₃⁻的去除率高达98%。线性扫描伏安法测试(LSV)结果表明, Cu催化剂相较于Fe₂O₃具有更正的NO₃⁻还原到NO₂⁻起始电位(0.39 V_{RHE}), 并在-0.2到-0.3 V_{RHE}区间里出现NO₂⁻积累的电流平台。由此可见, Cu对NO₃⁻的吸附和转化为NO₂⁻的能力相较于Fe₂O₃更为优异。然而由于Cu对*N的吸附能力较弱, 导致NO₂⁻更容易脱附并在表面积累。相比之下, Fe₂O₃在NO₂⁻溶液中的起始电位(>0.3 V_{RHE})远高于在NO₃⁻溶液中的起始电位(0.1 V_{RHE}), 表明其具有较强的*N吸附能力, 能够更有效地将NO₂⁻进一步还原为NH₃。原位拉曼和原位红外光谱分析进一步证实了NO₃⁻RR过程中中间体的生成, Cu上的NO₂⁻出现电位(0.3 V_{RHE})明显早于Fe₂O₃(0.1 V_{RHE})。Fe₂O₃上NO₂⁻和NH₃的起始电位相同(0.1 V_{RHE}), 而Cu-Fe₂O₃上NO₂⁻和NH₃的反应起始电位(0.4 V_{RHE})显著正于Cu和Fe₂O₃的反应起始电位, 这进一步证明了Cu将NO₃⁻还原为NO₂⁻, Fe₂O₃将NO₂⁻还原为NH₃的级联催化, 与LSV结论一致。

本文为NO₃⁻电还原提供了一种催化剂设计的新思路, 通过Cu-Fe₂O₃异质结构实现了更低的反应开启电位(0.4 V_{RHE})。在低工作电位下(-0.27 V_{RHE})实现了423 mA cm⁻²的电流密度, 接近100%的NH₃选择性和98%的NO₃⁻转化率, 展现了该级联催化剂在可持续NH₃合成和废水处理中的潜力。

关键词: 电催化; 起始电位; 硝酸盐还原成氨; 级联催化; 异质界面

收稿日期: 2024-09-14. 接受日期: 2024-11-04. 上网时间: 2025-01-10.

*通讯联系人。电子信箱: miaozhong@nju.edu.cn(钟苗)。

基金来源: 国家自然科学基金(22272078, 22409087); 催化基础国家重点实验室开放基金(2024SKL-A-016); 江苏省“双创人才”计划。